

Chaotic behavior of three interacting vortices in a confined Bose-Einstein condensate

Nikos Kyriakopoulos

*SUPA, Department of Physics and Institute for Complex Systems and Mathematical Biology,
King's College, University of Aberdeen, Aberdeen, AB24 3UE, UK*

Vassilis Koukouloyannis

Physics Department, Aristotle University of Thessaloniki, GR-54124, Thessaloniki, Greece

Charalampos Skokos

*Department of Mathematics and Applied Mathematics,
University of Cape Town, Rondebosch, 7701, South Africa and
Physics Department, Aristotle University of Thessaloniki, GR-54124, Thessaloniki, Greece*

Panayotis Kevrekidis

Department of Mathematics and Statistics, University of Massachusetts, Amherst MA 01003-9305, USA

Motivated by recent experimental works, we investigate a system of vortex dynamics in an atomic Bose-Einstein condensate (BEC), consisting of three vortices, two of which have the same charge. These vortices are modeled as a system of point particles which possesses a Hamiltonian structure. This tripole system constitutes a prototypical model of vortices in BECs exhibiting chaos. By using the angular momentum integral of motion we reduce the study of the system to the investigation of a two degree of freedom Hamiltonian model and acquire quantitative results about its chaotic behavior. Our investigation tool is the construction of scan maps by using the Smaller ALignment Index (SALI) as a chaos indicator. Applying this approach to a large number of initial conditions we manage to accurately and efficiently measure the extent of chaos in the model and its dependence on physically important parameters like the energy and the angular momentum of the system.

I. INTRODUCTION

The study of two-dimensional particle dynamics resulting from a logarithmic interaction potential is a theme of broad and diverse interest in Physics. Arguably, the most canonical example of both theoretical investigation and experimental relevance is the exploration of fluid and superfluid vortex patterns and crystals, as is evidenced e.g. by the review of Aref et al. [1] and the book of Newton [2]. However, numerous additional examples ranging from electron columns in Malmberg-Penning traps [3] to magnetized, millimeter sized disks rotating at a liquid-air interface [4, 5] are also characterized by the same underlying mathematical structure and hence present similar dynamical features.

In recent years, the field of atomic Bose-Einstein condensates (BECs) [6, 7] has offered an ideal playground for the realization of a diverse host of configurations showcasing remarkable vortex patterns and dynamics. The early efforts along this direction principally focused on the existence and dynamical robustness/stability properties of individual vortices (including multi-charge ones that were generically identified as unstable in experiments), as well as of large scale vortex lattices created upon suitably fast rotation [8–11]. Some of the early theoretical and experimental efforts also touched upon few-vortex crystals [12, 13]. Yet, it was not until the development of more recent experimental techniques, such as the minimally destructive imaging [14–16], the imaging of dragged laser beams through the BEC [17], or the quadrupolar excitations spontaneously producing multi-vortex states [18] that few-vortex dynamics drew a sharp focus of the research effort. It is worthwhile to note that in this BEC context, some of the standard properties and conservation laws of the vortex system [19] still apply, including e.g. the angular momentum (i.e., the sum of the squared distances of the vortices from the trap center multiplied by their respective topological charge) or the Hamiltonian of the vortex system. However, others such as the linear momentum are no longer preserved. This is due to the local vortex precession term arising in the dynamics as a result of the presence of the external (typically parabolic) trap [8, 9].

Motivated by the ongoing experimental developments, and perhaps especially the work of Seman et al. [18], in the recent work of Koukouloyannis et al. [20], a detailed study of the transition from regular to progressively chaotic behavior has been performed in the tripole configuration (consisting of two vortices of one circulation and one of the opposite circulation). This has been achieved by using a sequence of Poincaré sections with the angular momentum L of the vortex system as a parameter. Notice that while this tripole system without the local BEC-trap induced precession is integrable (see e.g. the discussion of Aref and co-workers [19, 21]), here the absence of linear momentum conservation renders chaotic dynamics accessible at this level. In this context the main bifurcations which lead to the destabilization of the system and the eventual appearance of chaotic behavior have been observed. Our aim in the present work is to provide more quantitative results about the chaotic behavior of the system for various energy levels. As a principal tool to this effect, we will employ an efficient chaos detection method, the so-called Smaller ALignment Index (SALI).

Our study is structured as follows. In section II, we briefly present the setup of the theoretical particle model developed earlier [15, 16, 20], which we will use in the present study. In section III, we present the numerical tools that we use in this work, namely the chaoticity index SALI and the scan maps that can be derived by using this index. After that, in section IV.A we perform an extended dynamical study of the system for a typical value of its energy h by using its angular momentum L as a parameter. In this study we concentrate mainly in the study of the evolution of the permitted area of motion and the chaoticity of the system as the value of L varies. In addition, based on some physical properties of our system we argue that SALI is a more relevant tool of investigation for this study than the maximum Lyapunov exponent (mLE). In section IV.B we generalize this study in order to acquire a more global picture of the dynamics of the system by including most of the physically meaningful values of the energy of the system. Finally, we summarize our findings and present some directions for future study in section V.

II. THE MODEL

In this section we briefly present the model used also in Koukouloyannis et al. [20] for the study of the dynamical behavior of a system of three interacting vortices in quasi-two-dimensional (pancake shaped) BEC. We consider two of them having the same topological charge $S_1 = S_3 = 1$ while the third has $S_2 = -1$, following the experimental results of Seman et al. [18]. In this case, if the vortices are well-separated, they can be considered as point quasi-particles and the corresponding normalized equations describing their motion are

$$\begin{aligned} \dot{x}_i &= -S_i \frac{y_i}{1 - r_i^2} - c \sum_{j=1, j \neq i}^N S_j \frac{y_i - y_j}{r_{ij}^2} \\ \dot{y}_i &= S_i \frac{x_i}{1 - r_i^2} + c \sum_{j=1, j \neq i}^N S_j \frac{x_i - x_j}{r_{ij}^2} \quad i, j = 1, 2, 3. \end{aligned} \tag{1}$$

where (x_i, y_i) stand for the coordinates of the i -th vortex in the plane of motion, while $r_i = \sqrt{x_i^2 + y_i^2}$ and $r_{ij} = \sqrt{(x_i - x_j)^2 + (y_i - y_j)^2}$. The parameter c is connected to the physical properties of the BEC and a typical value for it has been estimated e.g. by Navarro et al. [16] to be $c \approx 0.1$. The above equations have been rescaled so the Thomas-Fermi radius of the BEC (which characterizes the radial extent of the BEC) is $R_{TF} = 1$. Consequently, $0 \leq r_i < 1$.

This system can be described by a three degrees of freedom Hamiltonian, where each pair of coordinates (x_i, y_i) corresponds to one degree of freedom. The above equations of motion, for the particular choice of S_1, S_2, S_3 can be derived by the Hamiltonian

$$H = \frac{1}{2} \sum_{i=1}^3 \ln(1 - r_i^2) + \frac{c}{2} [\ln(r_{12}^2) - \ln(r_{13}^2) + \ln(r_{23}^2)] \quad (2)$$

via the canonical equations $\dot{x}_i = S_i \frac{\partial H}{\partial y_i}$, $\dot{y}_i = -S_i \frac{\partial H}{\partial x_i}$. Considering $\mathbf{q} = (x_1, y_1, x_2, y_2, x_3, y_3)$, $\mathbf{p} = (p_1, p_2, p_3, p_4, p_5, p_6)$ we acquire the usual form of the canonical equations $\dot{q}_i = \frac{\partial H}{\partial p_i}$, $\dot{p}_i = -\frac{\partial H}{\partial q_i}$ for the system's evolution.

Applying two successive canonical transformations: a) $(x_i, y_i) \mapsto (w_i, R_i)$ defined by

$$q_i = \sqrt{2R_i} \sin(w_i), \quad p_i = \sqrt{2R_i} \cos(w_i), \quad i = 1 \dots 3, \quad (3)$$

and b) $(w_i, R_i) \mapsto (\phi_{1,2}, \vartheta, J_{1,2}, L)$ according to

$$\begin{aligned} \phi_1 &= w_1 - w_3 & J_1 &= R_1 \\ \phi_2 &= w_2 + w_3 & J_2 &= R_2 \\ \vartheta &= w_3 & L &= R_1 - R_2 + R_3, \end{aligned} \quad (4)$$

the Hamiltonian (2) assumes the form

$$\begin{aligned} H &= \frac{1}{2} [\ln(1 - 2J_1) + \ln(1 - 2J_2) + \ln(1 - 2(L - J_1 + J_2))] \\ &+ \frac{c}{2} \left[\ln(4J_2 - 2J_1 + 2L - 4\sqrt{J_2}\sqrt{L - J_1 + J_2} \sin(\phi_2)) \right. \\ &\quad \left. - \ln(2L + 2J_2 - 4\sqrt{J_1}\sqrt{L - J_1 + J_2} \cos(\phi_1)) \right. \\ &\quad \left. + \ln(2J_1 + 2J_2 - 2\sqrt{J_1}\sqrt{J_2} \sin(\phi_1 + \phi_2)) \right]. \end{aligned} \quad (5)$$

Since the above Hamiltonian is autonomous, the *energy* of the system, which is expressed by H , is conserved. In addition, ϑ is ignorable and consequently its conjugate generalized momentum L (4), the *angular momentum* of the system, is also an integral of motion. Thus, Hamiltonian (5) can be considered as a two degrees of freedom system with L as a parameter.

In what follows we use the value of the energy h of the system and the value of the angular momentum L as the main parameters of our study. Both values depend on the particular vortex configuration, i.e. the set of initial conditions of each orbit as $h = H(x_{10}, y_{10}, x_{20}, y_{20}, x_{30}, y_{30})$ and $L = L(x_{10}, y_{10}, x_{20}, y_{20}, x_{30}, y_{30})$.

Before we present our main results, we will briefly discuss the numerical methods of this study.

III. NUMERICAL METHODS

A. The Smaller ALignment Index - SALI

The most commonly used chaos indicator is the computation of the maximum Lyapunov exponent (mLE) [22–24], which is based on the evolution of one deviation vector from the studied orbit. The main drawback for using the mLE is the long time needed for the index to converge to its limiting value, especially for chaotic orbits that stick close to regular ones for long times.

Many methods have been developed over the years that overcome this problem and allow the fast and reliable characterization of orbits as chaotic or regular, like the Fast Lyapunov Indicator (FLI) [25, 26] and its variants [27, 28], the Smaller (SALI) [29] and the Generalized (GALI) [30] ALignment Indices, the Mean Exponential Growth of Nearby Orbits (MEGNO) [31, 32], the Relative Lyapunov Indicator (RLI) [33, 34], the Frequency Map Analysis [35, 36], the

‘0-1 test [37, 38], and the Covariant Lyapunov Vectors (CLV) method [39, 40]. A concise presentation of some of these methods, as well as a comparison of their performances can be found in the works of Maffione et al.[41] and Darriba et al.[42]. In our study we will use the SALI method, which proved to be an efficient indicator of chaos. The SALI depends on the evolution of two initially different deviation vectors, which are repeatedly normalized from time to time and checks whether they will align (chaotic orbit) or not (regular orbit). It has been shown that SALI tends exponentially fast to zero for chaotic orbits, while it fluctuates around constant, positive values for regular ones[43, 44]. In practice, we require SALI to become smaller than a very small threshold value (in our study we set $\text{SALI}_{thres} = 10^{-12}$) to characterize an orbit as chaotic. The different behavior of the SALI for chaotic and regular orbits makes it an efficient chaos indicator, as its many applications to a variety of dynamical systems[45–56] illustrate. Thus, SALI constitutes an ideal numerical tool for the purposes of our study, as its computation for a large sample of initial conditions allows the construction of phase space charts (which we will call ‘scan maps’) where regions of chaoticity and regularity are clearly depicted and identified.

B. The scan map

In order to calculate a scan map we first have to define a Poincaré surface of section (PSS) [57]. Since our Hamiltonian is considered to be a two degrees of freedom one with L as a parameter, for the PSS to be defined we have to consider fixed values h and L for the energy and the angular momentum respectively. We also consider a constant value for ϕ_2 , namely $\phi_2 = \pi/2$. In this way the plane (ϕ_1, J_1) is defined as the plane of the PSS and J_2 is calculated at each point of the section by (5). Note that the value of $\phi_2 = \pi/2$ corresponds to the configuration where the S_2 and S_3 vortices lie on the half-line having the center of the condensate on its edge as can be seen from the transformations (3) and (4). The main motion of the vortices is dictated by their gyroscopic precession which has as a result vortices with opposite charge to rotate in different directions. Consequently, as we can see from (4), the angle ϕ_2 will take almost all the values, independently of the choice of the specific orbit. Thus, the section which corresponds to $\phi_2 = \pi/2$ is appropriate for revealing the system’s main dynamical features as it is crossed by the vast majority of the permitted orbits. Several PSSs obtained by this approach, for $h = -0.7475$ and various values of L are seen in the upper panels of FIG. 1.

In order to construct a scan map, like the ones shown in the lower panels of FIG. 1, we select an equally spaced grid of 300×300 initial conditions (ϕ_1, J_1) on the PSS and compute SALI for each orbit[58]. When the value of SALI becomes $\text{SALI} < \text{SALI}_{thres} = 10^{-12}$ we consider SALI to practically be zero and the corresponding orbit to be chaotic. We denote the time needed for an orbit to reach this threshold $t_{S_0}(\phi_{10}, J_{10})$. The maximum integration time we consider is $t_{max} = 3000$. If $\text{SALI}(t_{max}) > \text{SALI}_{thres}$ then the orbit is considered to be regular. In that case, we set t_{S_0} to be $t_{S_0} = t_{max}$. Depending on the value of $t_{S_0}(\phi_{10}, J_{10})$, we assign a color to each point of the grid. In particular, darker colored points correspond to orbits with smaller t_{S_0} , while lighter colored points correspond to orbits with larger t_{S_0} . In this way we construct color charts of the PSS based on how fast the chaotic nature of an orbit is revealed. These scan maps clearly show not only the regions where regular and chaotic motion occurs, as the comparison with the PSS plots in the upper panels of FIG. 1 easily verifies, but also indicate regions with different degrees of chaoticity. Finer grids and longer integration times were also considered, but the results they provided were not significantly different from the ones presented in FIG. 1, while the additional computational time required was extremely longer. Hence, the choice of the 300×300 grid and the value $t_{max} = 3000$ have been deemed to be the most efficient in order to reveal the details of the dynamical behavior of this system.

IV. RESULTS

A. Dynamical behavior of the system for $h=-0.7475$

The dynamical behavior of Hamiltonian (5) has been studied in Koukouloyannis et al.[20] for the value of the energy $h = -0.7475$ and increasing values L of the angular momentum. This behavior is summarized in FIG. 1, where various PSSs are shown together with the corresponding scan maps. This value of h refers to a ‘typical’ configuration of the system i.e. a configuration where the vortices are well separated and not close to the Thomas-Fermi radius. As it can be seen from (4), since $0 < R_i < 0.5$ the typical range of the values of L is $-0.5 < L < 1$. But, since the energy constraint must also be fulfilled, the range is actually smaller. In particular, for $h = -0.7475$ the range considered is $-0.45 \leq L \leq 0.55$.

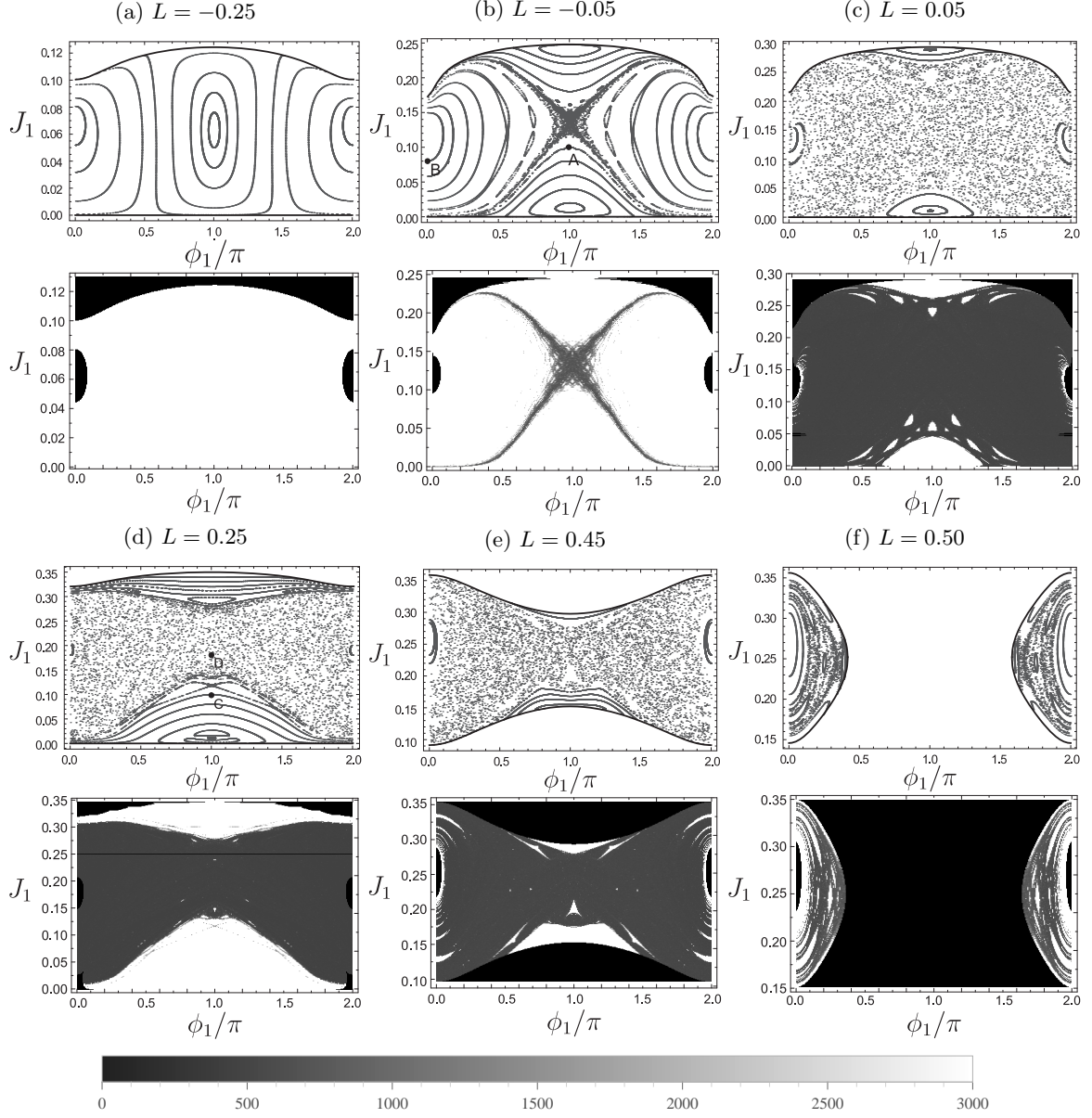


FIG. 1: Poincaré surfaces of section (upper panels) and the corresponding SALI scan maps (lower panels) of Hamiltonian (5) for energy $h = -0.7475$ and varying values of L . In the PSSs the thick black curves correspond to boundaries of motion. In the scan maps the black areas correspond to non-permitted orbits. The gray scale shown below the panels is used for coloring each permitted initial condition according to its t_{S_0} value (see text for more details). So, dark colored points correspond to orbits with small t_{S_0} (chaotic orbits) and light colored points correspond to orbits with large t_{S_0} (regular orbits). In the upper plots of panels (b) and (d) the initial conditions of some particular orbits studied in Sect. IV A are also indicated.

For values $L < -0.218$ the system is fully organized featuring only regular orbits as it can be seen in FIG. 1(a). For a critical value of $L \simeq -0.218$ the central periodic orbit destabilizes through a pitchfork bifurcation, and a chaotic region is subsequently created (FIG. 1(b)). This region gets wider as L increases (FIG. 1(c)). For even larger values of L , the permitted area of the PSS shrinks, as we will see in detail later on, (FIG. 1(e)–(f)) and finally all the allowed configurations of the system correspond to regular orbits which are concentrated around an orbit involving the collision of the vortices $S_1 - S_3$.

In the corresponding scan maps we observe some black areas which represent rejected initial conditions of the grid. There are three reasons to reject an initial condition on the PSS. The first is that the specific point does not comply with both the energy and angular momentum constraints of the system. These are the upper and lower black areas

in the lower panels of FIG. 1(a)–(e) and the large, central, black area of FIG. 1(f). The second reason to exclude an initial condition is if a particular configuration corresponds to a collision orbit, i.e. two vortices lie at the same point of the configuration space $(x - y)$. This state is meaningless both physically and mathematically, since the energy of the system becomes infinite. This case is visible in FIG. 1(d) where a horizontal black line is shown at $J_1 = 0.25$, which corresponds to a collision between S_2 and S_3 . The third reason is purely physical: if the initial condition represents a configuration in which the two co-rotating vortices S_1 and S_3 lie close to each other, these two vortices become ‘trapped’ in a motion where they rotate around each other. This is called the ‘satellite’ regime. Additionally, if the distance between them is too small ($r_{13} < 0.1$), our model does not describe the dynamics accurately, as it was constructed under the assumption that vortices behave like particles retaining their structure unchanged, which of course is not true when they acquire this level of proximity. So in our study we do not try to tackle questions related to close encounters of the vortices. This restriction corresponds to the small black areas on the left and right end sides of the scan maps. In this consideration we have not excluded the cases where the counter-rotating vortices come close to each other since in this case they are not trapped but instead they just pass by each other and continue their motion.

In this work we are interested, not only to see the general dynamical behavior of the system, but in acquiring more quantitative results, than the ones described above, concerning the permitted area of motion and the chaoticity percentages of the system.

1. Permitted area of motion

The boundaries of the permitted areas in FIG. 1 are calculated by the requirement that one of the vortices will pass through the origin [20] ($R_i = 0$). From the transformation (4) we see that R_2 has a negative contribution to L , while R_1 and R_3 contribute positively. Thus, for low values of L , the S_2 vortex is moving away from the origin and the boundaries are determined by the $R_1 = 0$ and $R_3 = 0$ constraints. In particular, the former condition provides the $J_{1_{lo}}(R_1=0) = 0$ boundary, while the latter gives $J_2 = J_1 - L$. Since in each panel of FIG. 1 we consider fixed values for h and L and in addition we set $\phi_2 = \pi/2$ for the construction of the PSSs, Hamiltonian (5) provides an implicit relation $J_{1_{up}}(R_3=0) = J_{1_{up}}(\phi_1; h, l)$ for the upper boundary of the permitted area. On the other hand, for high values of L the $J_{1_{lo}}(R_2=0)$ and $J_{1_{up}}(R_2=0)$ boundaries are both calculated by the constraint $R_2 = 0$, through similar considerations.

The permitted area can now be numerically calculated by the integral

$$A_p = \int_0^{2\pi} (J_{1_{up}} - J_{1_{lo}}) d\phi_1. \quad (6)$$

In (6), each point of $J_{1_{up}}$ and $J_{1_{lo}}$ is also calculated numerically through the implicit functions $J_{1_{up}}(\phi_1)$ and $J_{1_{lo}}(\phi_1)$ mentioned above. The obtained results are reported in FIG. 2 by a solid line. For intermediate values of L , just after the maximum of the curve $A_p = A_p(L)$, there is an ambiguity concerning whether the boundary is determined by the constraint $R_3 = 0$ or $R_2 = 0$, because for some values of ϕ_1 the boundary is defined by the former, while for others it is defined by the latter relation. In this region we cannot calculate the size of the permitted area by (6) and the calculation from the PSSs is more reliable. In this case we estimate the size of the permitted area as the sum of the areas of all the small rectangles of the grid on the PSS, which is also used in the scan maps, and correspond to permitted orbits. The obtained results are depicted by dots in FIG. 2. The two well computed by (6) parts of $A_p(L)$ are connected in this region by a dashed straight line in order to obtain a continuous curve. It is worth noting that even this rough approximation is in good agreement with the results obtained by counting the permitted initial conditions on the PSS. The good agreement of the results obtained by these two approaches indicates that the used grid of initial conditions is satisfactorily dense for capturing the dynamics of the system.

2. Regular and Chaotic configurations

The chaotic or regular behavior of an orbit depends on the configuration (initial position in the $x - y$ plane of the BEC) of the vortices. In FIG. 3 the configurations which correspond to orbits on the PSS which exhibit regular motion are shown. Since these configurations correspond to initial conditions with $\phi_2 = \pi/2$ the S_2 and S_3 vortices lie on the same half-line, while the S_1 vortex can occupy various positions. The initial positions of the S_1 , S_2 and S_3 vortices are depicted in these figures by red, green and blue color respectively. The permitted area of motion of the S_1 vortex is defined by thick black lines. In general the vortices in the BEC can move up to the Thomas-Fermi radius, which is equal to $R_{TF} = 1$, but since we have fixed values of h and L the actual permitted area is smaller.

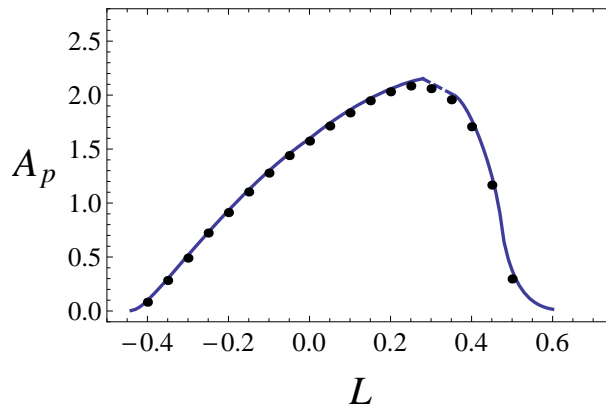


FIG. 2: The permitted area of motion for $h = -0.7475$ shown as a function of L . The solid line represents the calculation of the area using (6). The dots represent the results obtained by estimating the size of the permitted area as the sum of the areas of all the small rectangles of the grid of the PSS which correspond to permitted orbits. The dashed line connecting the two parts of the solid curve corresponds to the region of the values of L in which there is an ambiguity in the calculation of the area through (6) discussed in the text.

In FIG. 3 (in direct comparison also with FIG. 1) it is shown that for small values of L almost all of the permitted area is occupied by regular orbits. As L increases, almost all of the available configurations are chaotic, for $L = 0.25$ the percentage of the chaotic orbits presents a local minimum and for values of $L > 0.45$ the permitted area shrinks significantly and almost all the orbits become regular.

Let us look a bit closer at the relation between the initial configuration of the vortices and the system's dynamical behavior by studying in more detail three representative cases.

We start our analysis by considering $L = -0.05$ for which almost all initial vortex configurations (or initial conditions) lead to regular motion (see FIG. 1(b) and FIG. 3(a)). In FIG. 4(a) we consider an ensemble of initial configurations in order to check the motion corresponding to it. In FIG. 4(b) the time evolution of a representative orbit with $\phi_1 = \pi$ and $J_1 = 0.1$ is shown. The initial condition of this orbit corresponds to point A in the PSS of FIG. 1(b). This is the case of the 'rotational' regime where all the vortices rotate around the common center of rotation without any major disturbances to their motion, producing regular behaviors. As we can see, the areas the orbits of the individual vortices occupy are distinct and do not mix. In this case the vortices interact weakly with each other and they are said to be at the so-called 'one-vortex' regime. In general, when an initial configuration produces evolutions belonging to the one-vortex regime the resulting motion is regular.

The second case we examine is shown in FIG. 5. In this case the S_1 and S_3 vortices rotate around each other and both of them around the center of rotation. The S_2 vortex rotates around the center as well but in the opposite direction because of its opposite charge. This is the so-called 'satellite' regime. In this case the two vortices interact more strongly with each other while they exhibit a weak interaction with the third one. As we can see in FIG. 5(b) the areas of trajectories of S_1 and S_3 cover overlap but do not mix with the one of S_2 . This dynamical regime is referred as the 'two-vortex' regime which also results in regular motion. The corresponding initial conditions of this orbit are depicted in the PSS of FIG. 1(b) by the point B.

The next case we consider is the one with $L = 0.25$. For this value of L numerous chaotic as well as regular initial configurations exist. In FIG. 6(a) the regular initial configurations for $J \leq 0.1$ are depicted. In FIG. 6(b) the time evolution of a representative orbit of this ensemble with $\phi_1 = \pi$ and $J_1 = 0.1$ is depicted. The initial condition of this orbit is depicted in the upper panel of FIG. 1(d) as point C. The trajectories of the vortices clearly correspond to the 'two-vortex' regime since only two of them interact strongly. On the other hand in FIG. 6(c) the time evolution of an initial configuration with $\phi_1 = \pi$ and $J_1 = 0.18$ leading to chaotic motion is shown. The initial condition is shown in FIG. 1(d) as point D. Here the strong interaction between all the vortices, which is generally necessary in order to have chaotic motion, can be concluded by the fact that the orbits of all the vortices mix with each other.

3. Consideration of an alternative t_{max} based on the physical aspects of the system

Let us now study in more detail the system's chaotic behavior. Since the physical model from which this study has been motivated is a Bose-Einstein condensate, which has a limited life time (commonly of the order of a few seconds to a few tens of seconds), there are some associated considerations to be kept in mind. In particular, in our set up

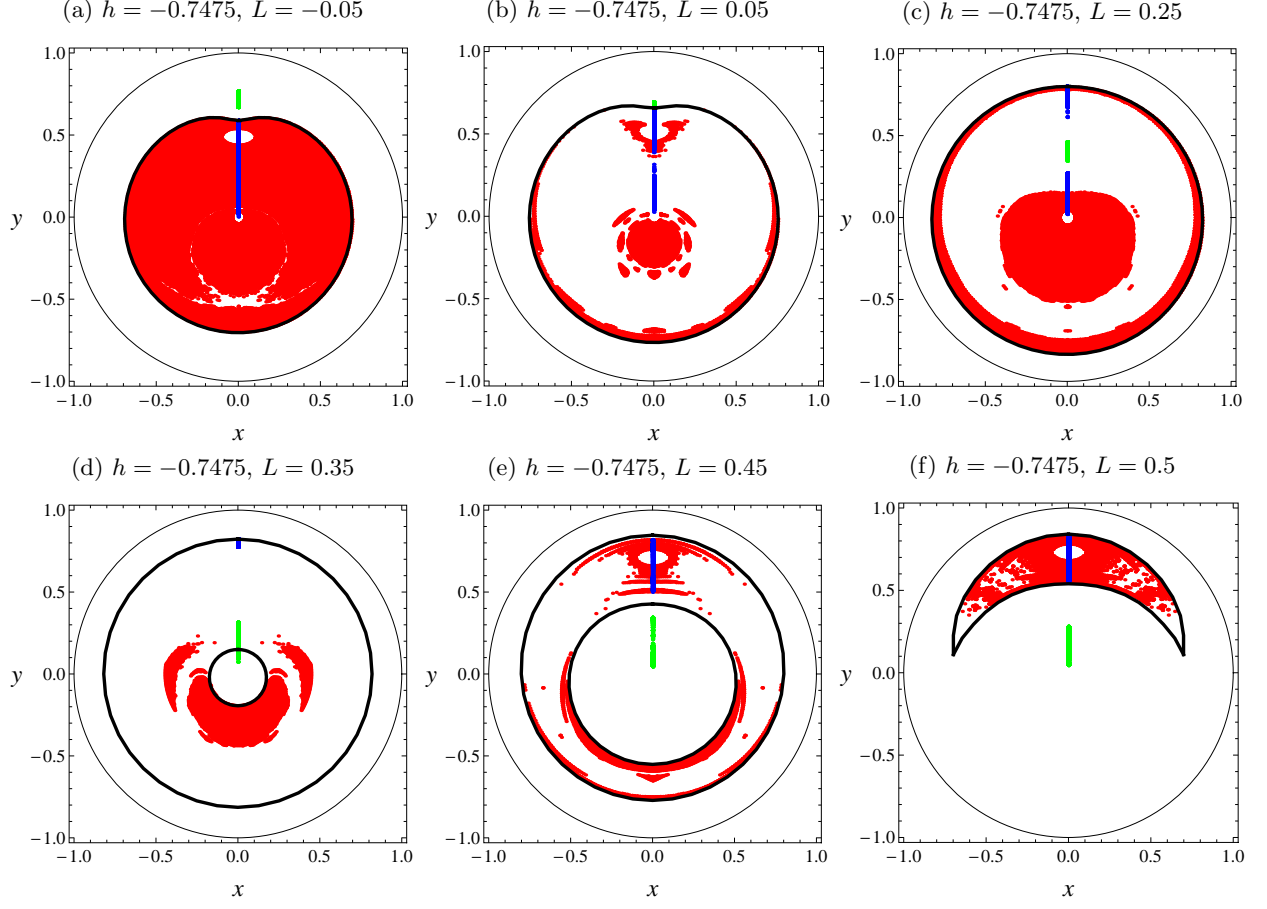


FIG. 3: Initial configurations which result to regular motion for $h = -0.7475$ and various values of L . The initial positions of S_1 , S_2 and S_3 vortices are represented by red, green and blue color respectively. Since the configurations correspond to orbits on the PSS ($\phi_2 = \pi/2$) the S_2 and S_3 vortices lie on the same semi-axis and some of the green dots may be indistinguishable. The permitted area of motion of S_1 is depicted by a thick black line. It can be easily seen that it is smaller than the disk defined by the Thomas-Fermi radius $R_{TF} = 1$.

the condensate's life time is of the order of a few hundreds up to one thousand time units.

We thus need to explore the implications that this physically induced time limit has. In order to address this question we consider in FIG. 7 the scan map for $h = -0.7475$ and $L = -0.03$. This map was constructed similarly to the ones of FIG. 1. The connected chaotic region in the center of this plot (dark gray points) can be constructed by any orbit starting in it. Nevertheless, depending on where we choose the initial condition of this orbit, the time in which its chaotic behavior is revealed varies. This becomes evident from the results of FIG. 8 where the plot of FIG. 7 is decomposed into four regions depending on the t_{S_0} values of the initial conditions. In particular we consider points with $t_{S_0} \in [140, 500]$ (FIG. 8a), $t_{S_0} \in (500, 1000]$ (FIG. 8b), $t_{S_0} \in (1000, 1500]$ (FIG. 8c) and $t_{S_0} \in (1500, 2000]$ (FIG. 8d). From these figures we can conclude that as we move further from the center of the x-shaped region the orbits become 'stickier' and thus they require more time to reveal their chaotic nature. These orbits involve predominantly two-vortex dynamics during earlier stages of the evolution, while at later stages all three vortices are interacting with each other, leading to the associated observed chaotic features. Since the typical lifetime of the BEC is a few hundred time units, a good candidate for a physically meaningful integration time would be $t_{max} = 500$. In this way, chaotic orbits which reveal their nature later than this time can be considered, from a practical point of view, as regular. For instance, in real experiments one would expect to detect chaotic motion in the limited time that the experiment lasts, only in regions with small t_{S_0} . In our case, such orbits are the ones plotted in FIG. 8(a), whose initial conditions are located close to the center of the x-shaped chaotic region. Thus, the need for efficient chaos indicators, capable of determining the nature of the orbits in potentially shorter, physically meaningful time intervals is of considerable importance. The SALI can successfully play this role, since it can reveal the larger part of the chaotic region of the system, even for $t_{S_0} = 500$, as can be seen in FIG. 8 and will be also shown in the next

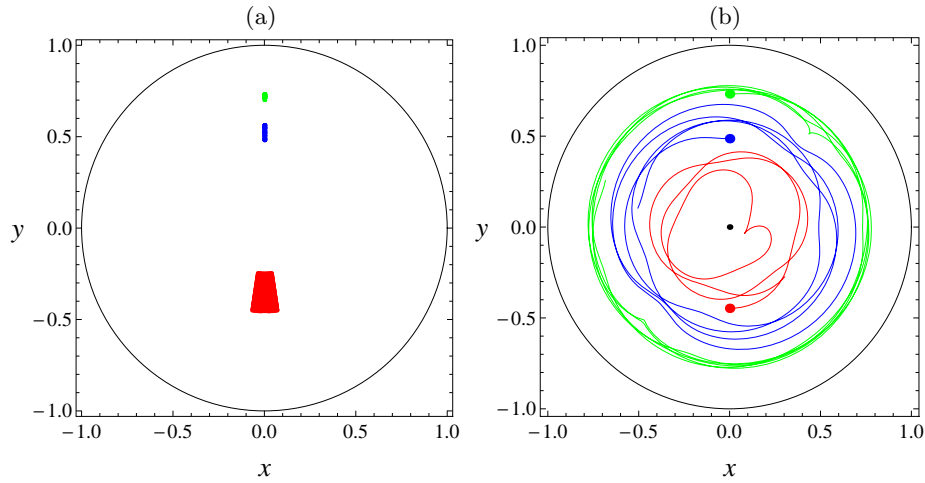


FIG. 4: (a) A fraction of the regular initial configurations in the $L = -0.05$ case which corresponds to the ‘rotational’ regime. (b) The time evolution of a representative orbit of this regime with $\phi_1 = \pi$ and $J_1=0.1$. We can see that the trajectories do not intersect each other, so the dynamics belongs to the ‘one-vortex’ regime.

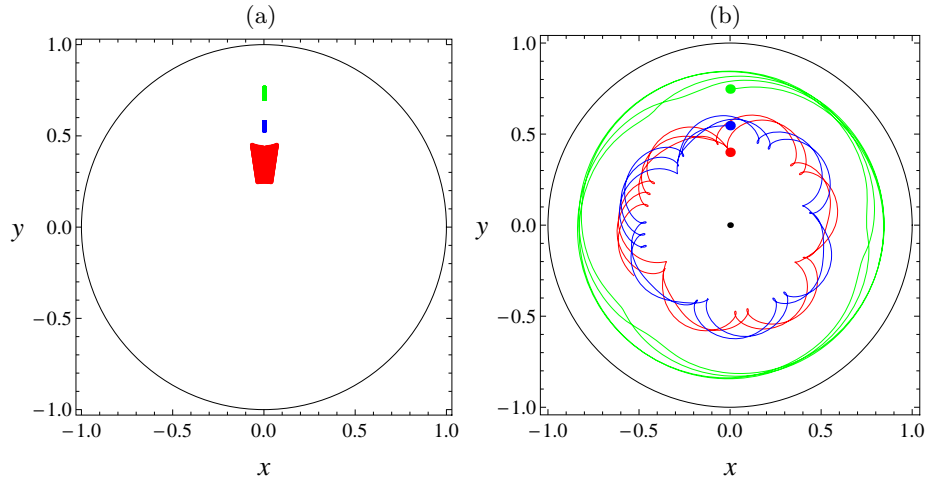


FIG. 5: (a) A fraction of the regular initial configurations in the $L = -0.05$ case which corresponds to the ‘satellite’ regime. (b) The time evolution of a representative orbit of this regime with $\phi_1 = 0$ and $J_1=0.08$. We can see that S_1 and S_3 interact strongly with each other but their orbits do not intersect that of S_2 , so we are inside the ‘two-vortex’ regime.

section through FIG. 9. On the other hand the mLE would require at least an order of magnitude larger integration times in order to acquire decisive results, which is both physically irrelevant and CPU-time consuming.

In what follows we will both use $t_{max} = 3000$ in order to reveal the full dynamics of the system and $t_{max} = 500$ in order to determine its ‘practical’ dynamical behavior. The different choices of t_{max} will be clearly indicated.

4. Chaoticity Percentages

In order to have a complete picture of the evolution of the chaotic region for varying L we calculated, using the SALI, the percentage of the chaotic orbits over the permitted ones (FIG. 9). For this calculation we used both $t_{max} = 500$ as well as $t_{max} = 3000$. We can see that the percentage of the chaotic region is larger when t_{max} is larger, since some of the sticky orbits are now characterized as chaotic, but the general behavior does not change significantly. By examining FIG. 3 the results of FIG. 9 can be easily understood. As was previously explained, for small L ($L \leq -0.05$) the initial configurations correspond to either the one- or the two-vortex regime, which leads to

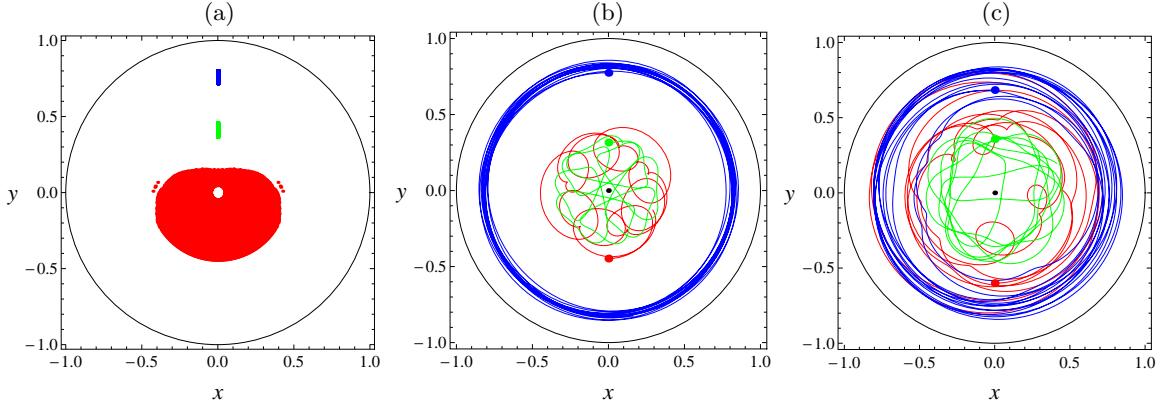


FIG. 6: (a) A fraction of the regular initial configurations in the $L = 0.25$ case which corresponds to $J_1 \leq 0.1$. (b) The time evolution of a representative orbit of this regime with $\phi_1 = \pi$ and $J_1 = 0.1$, which corresponds to a ‘two-vortex’ configuration. (c) The time evolution of the chaotic orbit with $\phi_1 = \pi$ and $J_1 = 0.18$. The trajectories of all vortices are mixing with each other, leading to chaotic behavior.

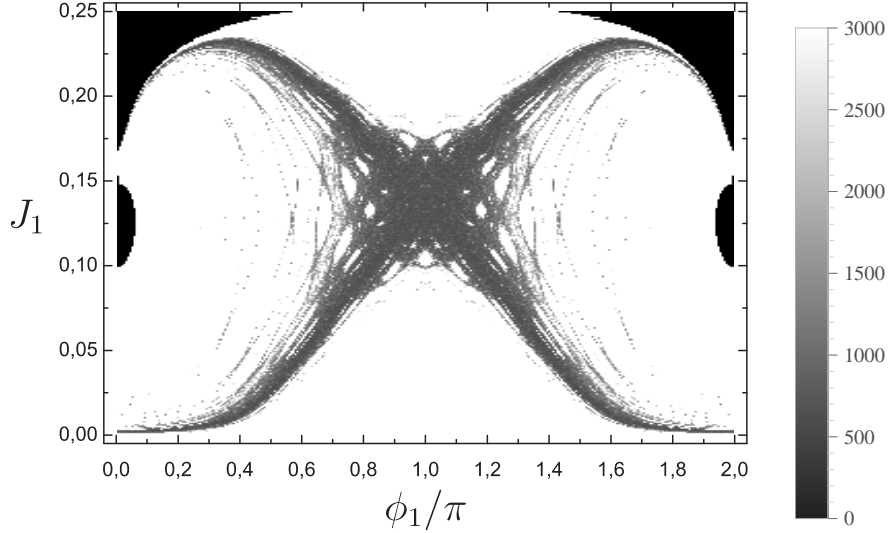


FIG. 7: Scan map for $h = -0.7475$ and $L = -0.03$. Dark colored points correspond to orbits with small t_{S_0} (chaotic) and light colored points correspond to orbits with large t_{S_0} (regular). This correspondence is also shown in the given legend.

regular motion. As L increases the orbit of either S_1 or S_3 lies further from the rotation center than before. There, it approaches the orbit of S_2 , causing strong interactions between all three vortices through slingshot effects, which result to a maximization of the chaotic region at $L = 0.05$. As the value of L increases further, one of the S_1 , S_3 vortices can lie far enough from the other two in order for the system to have two-vortex configurations, causing in this way the local minimum of the chaotic percentage for $L = 0.25$ observed in FIG. 9. At $L = 0.35$ we obtain a secondary maximum of the chaoticity percentage. This maximum corresponds to the range of L values just after the maximum of the permitted area (FIG. 2), where the ambiguity in the calculation of A_p occurs. This happens because at this L value the upper boundary of the permitted area is defined by both the $R_1 = 0, R_3 = 0$ and $R_2 = 0$ constraints, which means that the orbit of either S_1 or S_3 is close to the one of S_2 , causing again strong interactions between all three vortices and thus leading to chaotic behavior. For $L = 0.45$ both vortices with positive charge lie at a large distance from the center (nevertheless comparable to the one of S_2) but, at the same time, the permitted area of motion has decreased, which allows mainly configurations with strong interactions between all three vortices. This behavior leads to the maximization of the chaotic region. Finally, for even larger values of L ($L > 0.45$) the permitted area of S_1 and S_3 becomes very narrow and is located far away from the S_2 vortex, leading to two-vortex configurations and consequently to the minimization and eventual disappearance of the chaotic region.

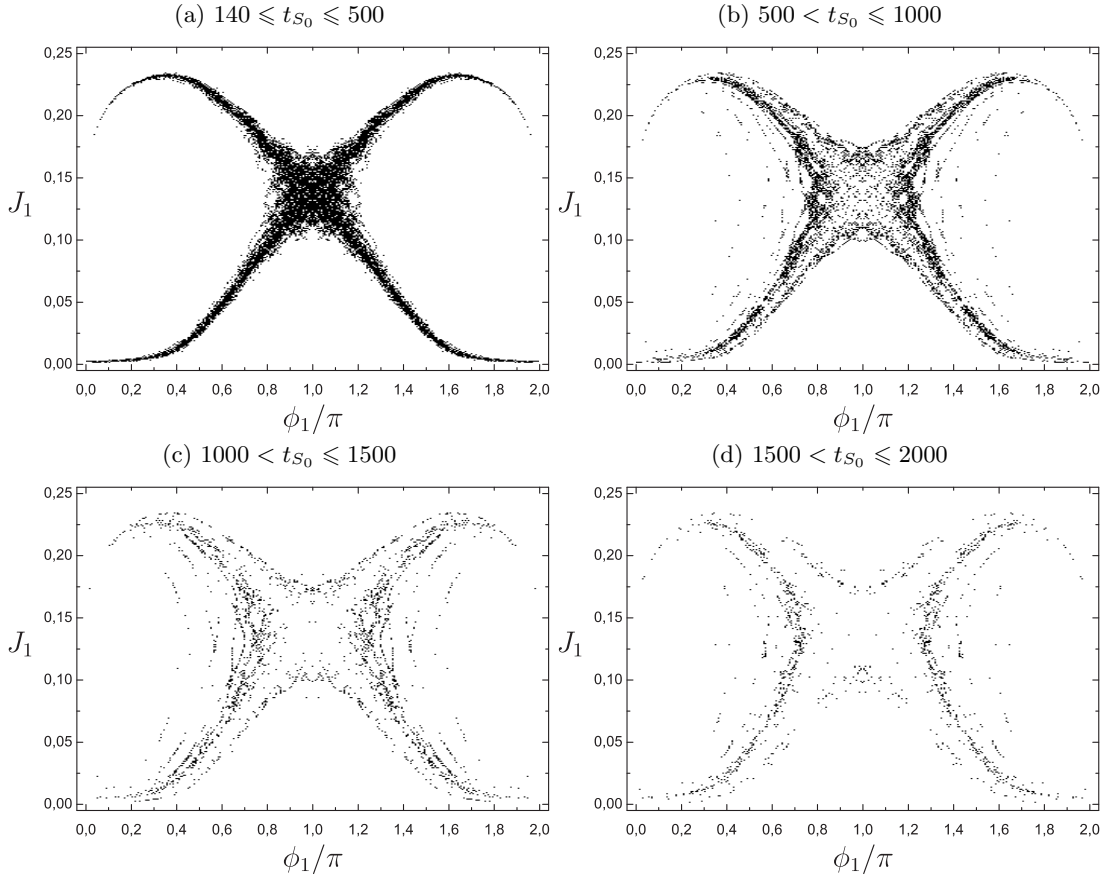


FIG. 8: The decomposition of FIG. 7 for various intervals of t_{S_0} . We see that as t_{S_0} increases the corresponding points of the scan map lie further away from the center of the x-shaped chaotic region and their number decreases.

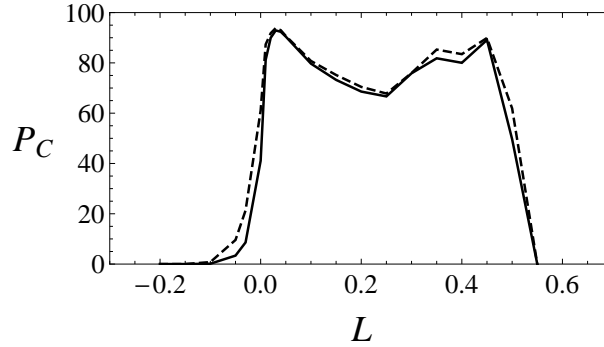


FIG. 9: The percentage P_C of initial conditions leading to chaotic orbits over the total number of permitted ones with respect to the value of L for $h = -0.7475$. The solid line represents the results for $t_{max} = 500$ while the dashed one corresponds to $t_{max} = 3000$. We observe that the main characteristics of P_C are the same in both cases.

B. Global Dynamics for $-1.1 \leq h \leq -0.5$

Based on the detailed analysis presented for the representative case of $h = -0.7475$ we perform a global study of the system's dynamical behavior for energy values in the range $-1.1 \leq h \leq -0.5$ in order to discover if the system exhibits similar behaviors. This range is assumed to contain all the physically meaningful energy values of the system.

a. Permitted area of motion. The calculations of the permitted areas of motion which are shown in FIG. 10 have been done in a similar way as the one described in section IV A 1. As we can see, the curves in all panels follow a similar pattern. For $L \lesssim -0.4$ no orbits exist, as no initial conditions satisfy both the h and L restrictions. As L increases (up

to $L \lesssim 0.15 - 0.35$ depending on h), the size of the permitted area grows larger as the $J_{1_{up}}(R_3=0)$ curve moves upwards in FIG. 1. For large values of L ($L \gtrsim 0.25 - 0.45$ depending on h) the boundaries are defined by the constraint $R_2 = 0$. As L increases even further, the permitted area shrinks because the boundaries defined by $J_{1_{up}}(R_2=0)$ and $J_{1_{lo}}(R_2=0)$ come closer. The dashed line corresponds to the intermediate values of L , where the ambiguity in the calculation of $A_p(L)$ occurs (as we also did in FIG. 2). Even for these values of L this rough approximation is again very close with the results obtained by the scan maps.

By examining the sequence of plots of FIG. 10(a)-(f) we conclude that the total area of permitted orbits decreases as h increases.

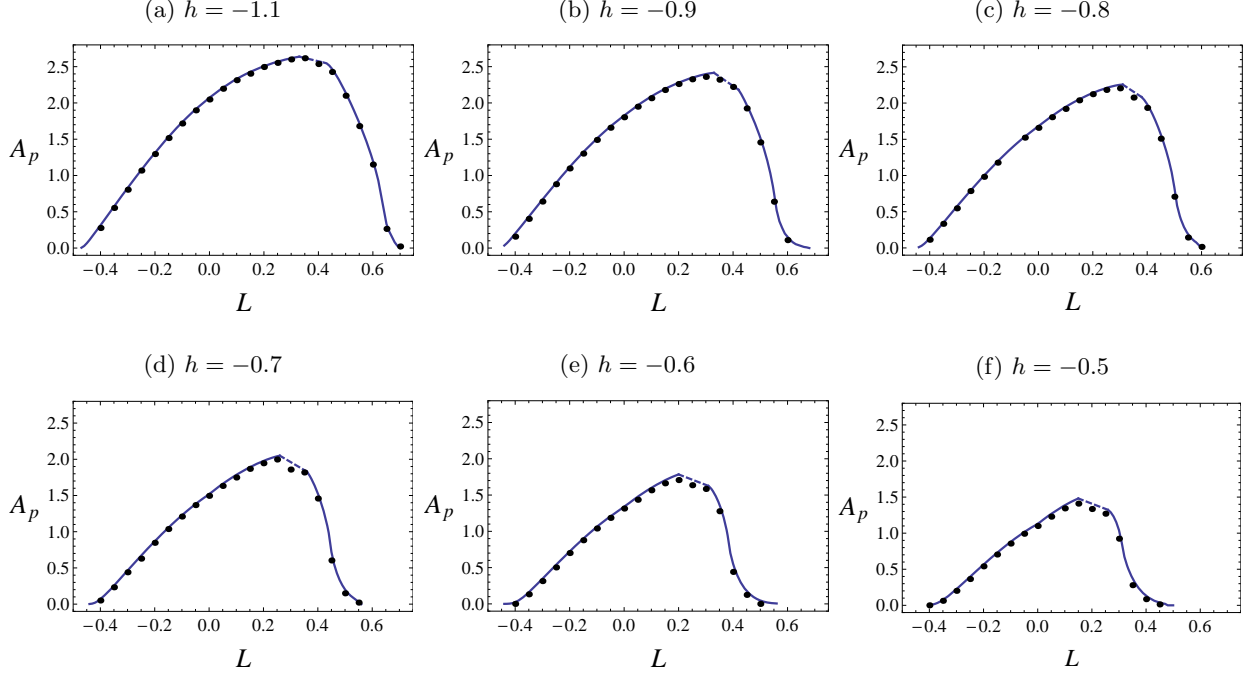


FIG. 10: Results similar to the ones of FIG. 2 for various values of h .

b. Chaoticity percentages. We calculate the percentage, P_C , of initial conditions leading to chaotic motion, within the set of the permitted initial conditions of the corresponding grid for $-1.1 \leq h \leq -0.5$ and $-0.2 \leq L \leq 0.6$, setting $t_{max} = 500$. The obtained results are plotted in FIG. 11 by solid lines. Again, resetting the final integration time to $t_{max} = 3000$ (dashed curves in FIG. 11) no significant differences are observed. The percentages slightly increase because some ‘sticky’ chaotic orbits are now characterized as chaotic, but apart from that the obtained curves are very close to the ones constructed for $t_{max} = 500$.

There seems to exist the same trend for all different values of the energy as already discussed in section IV.A.2 for $h = -0.7475$. For small values of the angular momentum ($L \lesssim -0.2$) no chaotic orbits exist. As L increases, P_C increases rather quickly and after an interval where it retains considerably high values, it drops down. Finally P_C vanishes for large values of L ($L \gtrsim 0.4 - 0.6$ depending on h), while at the same time the number of permitted initial conditions in the phase space shrinks (FIG. 10). The values of L for which the chaotic region appears (denoted L_c) and disappears (denoted L_d) depend on the particular value of the energy h . It is interesting to note that within this interval there is at least one local minimum, implying a local maximum in the fraction of regular trajectories.

Our results show that the range $L_d - L_c$ is larger for lower energies. This is related to the size of the permitted PSS area, which is also larger when h is smaller (FIG. 10). The appearance of the chaotic region seems to happen at about the same value $L \approx -0.1$, for all h values, but the eventual shrinking and disappearance of this region varies from $L_d \approx 0.4$ for $h = -0.5$ (FIG. 11(f)) to $L_d \approx 0.7$ for $h = -1.1$ (FIG. 11(a)). Presumably, the invariance of the onset of chaoticity is because of the weak h dependence on the critical value L_c for which the central stable periodic orbit undergoes a pitchfork bifurcation. This bifurcation generates the x-shaped chaotic region (FIG. 1(b)) which leads to the onset of chaoticity.

In addition, we observe smaller percentages of chaotic motion altogether for lower energies. While the maximum percentage for $h = -0.5$ is $\approx 100\%$ (FIG. 11(f)), the one for $h = -1.1$ is just $\approx 70\%$ (FIG. 11(a)). This behavior can be explained as follows. As we have seen in FIG. 10, the higher the energy of the vortices, the smaller the permitted

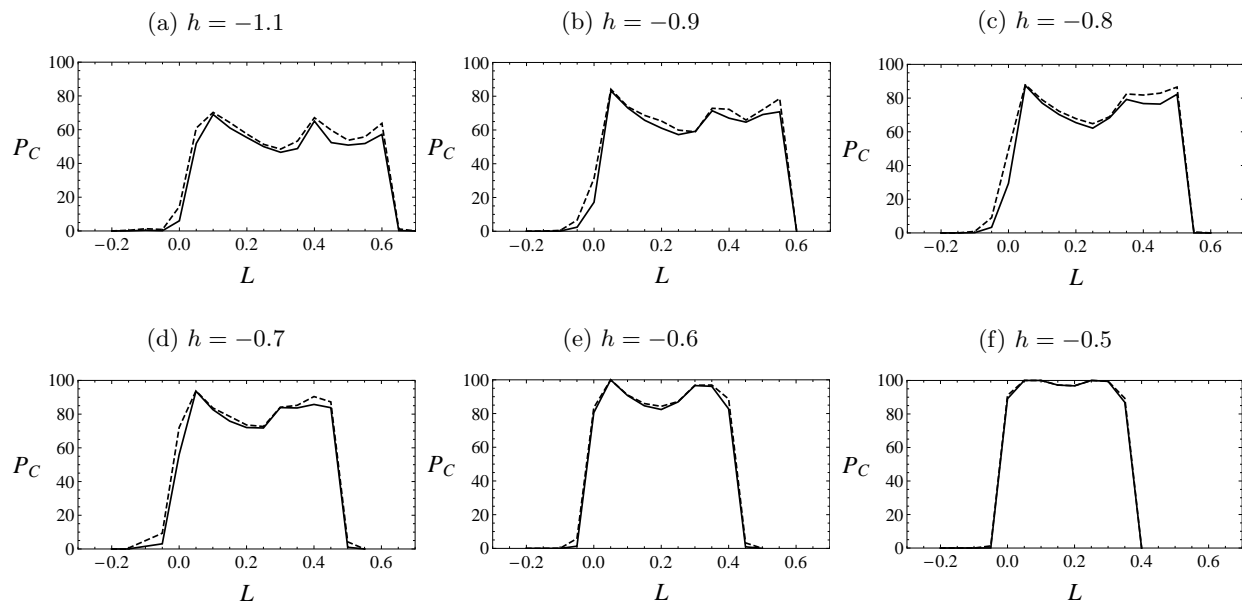


FIG. 11: Results similar to the ones of FIG. 9 for various values of h .

area of motion becomes. Consequently, the orbits of the vortices come closer and the interaction among all three of them becomes stronger, which in turn leads to the enhancement of the chaotic behavior.

We also observe in the panels of FIG. 11 that the ‘secondary’ local maximum between the two ‘main’ local maxima is more pronounced for low energies, for example it has the same height as the two ‘main’ maxima for $h = -1.1$ (FIG. 11(a)), while it becomes less distinct as the value of h increases, and practically disappears for $h = -0.5$ (FIG. 11(f)). This happens because, as the value of h increases, the overall percentages of the chaotic orbits increase. Consequently, this phenomenon becomes less significant and eventually not observable.

We believe that this analysis, based on the SALI, offers a systematic view of the PSS and the fraction of accessible orbits in it (as per FIG. 10), as well as of the fraction of chaotic orbits in it (as per FIG. 11) and how these change as a function of the canonical physical properties of the system, namely its energy and its angular momentum.

V. CONCLUSIONS - FUTURE DIRECTIONS

In the present work, we explored a theme of current interest within the research of atomic BECs, namely the recently realized experimentally tripoles of vortices and their associated nonlinear dynamical evolution. We found that this Hamiltonian system is arguably prototypical (at least within the realm of isotropic magnetic traps) in its exhibiting chaotic dynamics as parameters or initial conditions are varied. We focused here on the variation of initial conditions, through the variation of associated conserved quantities such as the energy and the angular momentum. Our aim was to associate a technique that has been previously used in a variety of other low dimensional settings, namely the SALI diagnostic, for efficiently measuring the chaoticity of the orbits within this atomic physics realm of vortex dynamics under their mutual interactions and their individual precession within the parabolic trap. We found that the SALI is a very accurate diagnostic of the different levels of chaoticity of the system and enables a qualitative understanding of how this chaoticity changes as the conserved quantities are varied, as well as a quantification of the chaotic fraction of the phase space of the system.

This work paves the way for the consideration of a wide range of additional problems within the dynamics of coherent structures in the realm of Bose-Einstein condensates. First of all, it would be straightforward to explore how the dynamics of this tripole would compare/contrast to the recently explored [16] dynamics of 3 co-rotating vortices (i.e., vortices of the same charge). Another natural extension in the vortex case would be to examine how the chaotic region expands as a fourth vortex of either a positive or a negative charge comes into play. The special cases of 4 co-rotating vortices (with relevant square and rhombic etc. stable configurations), as well as the case of the generally fairly robust [59] vortex quadrupole would be of interest in this setting. Additionally, extending such considerations to other dimensions would present interesting possibilities as well. On the one hand, a wide range of theoretical and experimental considerations (including particle based approaches, such as the ones utilized herein)

have been developed for dark solitons in 1d; see e.g. the recent review of Frantzeskakis [60]. On the other hand, generalizing to 3 dimensions and the consideration of multiple vortex rings and their dynamics [61] would be equally or even more exciting from the point of view of ordered vs. chaotic dynamics. Examination of these directions is currently in progress and will be reported in future publications.

ACKNOWLEDGMENTS

The authors would like to thank Prof. Roy H. Goodman for a comment that provided useful insights toward further development of this direction.

N.K. acknowledges support from the MC Career Integration Grant PCIG13-GA-2013-618399.

V.K. and Ch.S. have been co-financed by the European Union (European Social Fund - ESF) and Greek national funds through the Operational Program “Education and Lifelong Learning” of the National Strategic Reference Framework (NSRF) - Research Funding Program: THALES. Investing in knowledge society through the European Social Fund. Ch.S. was also supported by the Research Committees of the University of Cape Town (Start-Up Grant, Fund No 459221) and the Aristotle University of Thessaloniki (Prog. No 89317).

P.G.K. acknowledges support from the National Science Foundation under grants CMMI-1000337, DMS-1312856, from the Binational Science Foundation under grant 2010239, from FP7-People under grant IRSES-606096 and from the US-AFOSR under grant FA9550-12-10332.

-
- [1] H. Aref, P. K. Newton, M. A. Stremler, T. Tokieda, and D. L. Vainchtein, “Vortex crystals,” in *Advances in Applied Mechanics*, Vol. Volume 39 (Elsevier, 2003) pp. 1–79.
 - [2] P. K. Newton, *The N-Vortex Problem - Analytical Techniques* (Springer-Verlag, New York, 2001).
 - [3] D. Durkin and J. Fajans, “Experiments on two-dimensional vortex patterns,” *Physics of Fluids* (1994-present) **12**, 289–293 (2000).
 - [4] B. A. Grzybowski, H. A. Stone, and G. M. Whitesides, “Dynamic self-assembly of magnetized, millimetre-sized objects rotating at a liquid–air interface,” *Nature* **405**, 1033–1036 (2000).
 - [5] B. A. Grzybowski, H. A. Stone, and G. M. Whitesides, “Dynamics of self assembly of magnetized disks rotating at the liquid–air interface,” *Proceedings of the National Academy of Sciences* **99**, 4147–4151 (2002), PMID: 11929990.
 - [6] C. Pethick and H. Smith, *Bose-Einstein condensation in dilute gases* (Cambridge University Press, Cambridge; New York, 2008).
 - [7] L. P. Pitaevskii and S. Stringari, *Bose-Einstein condensation* (Clarendon Press, Oxford; New York, 2003).
 - [8] A. L. Fetter and A. A. Svidzinsky, “Vortices in a trapped dilute Bose-Einstein condensate,” *Journal of Physics: Condensed Matter* **13**, R135 (2001).
 - [9] A. L. Fetter, “Rotating trapped Bose-Einstein condensates,” *Reviews of Modern Physics* **81**, 647–691 (2009).
 - [10] P. K. Newton and G. Chamoun, “Vortex lattice theory: A particle interaction perspective,” *SIAM Review* **51**, 501–542 (2009).
 - [11] P. G. Kevrekidis, D. J. Frantzeskakis, and R. Carretero-González, *Emergent Nonlinear Phenomena in Bose-Einstein Condensates - Theory and Experiment* (Springer-Verlag, Berlin, 2008).
 - [12] Y. Castin and R. Dum, “Bose-Einstein condensates with vortices in rotating traps,” *The European Physical Journal D* **7**, 399 (1999).
 - [13] K. W. Madison, F. Chevy, W. Wohlleben, and J. Dalibard, “Vortex formation in a stirred Bose-Einstein condensate,” *Physical Review Letters* **84**, 806–809 (2000).
 - [14] D. V. Freilich, D. M. Bianchi, A. M. Kaufman, T. K. Langin, and D. S. Hall, “Real-time dynamics of single vortex lines and vortex dipoles in a Bose-Einstein condensate,” *Science* **329**, 1182–1185 (2010), PMID: 20813949.
 - [15] S. Middelkamp, P. J. Torres, P. G. Kevrekidis, D. J. Frantzeskakis, R. Carretero-González, P. Schmelcher, D. V. Freilich, and D. S. Hall, “Guiding-center dynamics of vortex dipoles in Bose-Einstein condensates,” *Physical Review A* **84**, 011605 (2011).
 - [16] R. Navarro, R. Carretero-González, P. J. Torres, P. G. Kevrekidis, D. J. Frantzeskakis, M. W. Ray, E. Altıntaş, and D. S. Hall, “Dynamics of a few corotating vortices in Bose-Einstein condensates,” *Physical Review Letters* **110**, 225301 (2013).
 - [17] T. W. Neely, E. C. Samson, A. S. Bradley, M. J. Davis, and B. P. Anderson, “Observation of vortex dipoles in an oblate Bose-Einstein condensate,” *Physical Review Letters* **104**, 160401 (2010).
 - [18] J. A. Seman, E. A. L. Henn, M. Haque, R. F. Shiozaki, E. R. F. Ramos, M. Caracanhas, P. Castilho, C. Castelo Branco, P. E. S. Tavares, F. J. Poveda-Cuevas, G. Roati, K. M. F. Magalhães, and V. S. Bagnato, “Three-vortex configurations in trapped Bose-Einstein condensates,” *Physical Review A* **82**, 033616 (2010).
 - [19] H. Aref, “Point vortex dynamics: A classical mathematics playground,” *Journal of Mathematical Physics* **48**, 065401 (2007).

- [20] V. Koukouloyannis, G. Voyatzis, and P. G. Kevrekidis, “Dynamics of three non-co-rotating vortices in Bose-Einstein condensates,” arXiv e-print 1309.6409 (2013).
- [21] H. Aref, N. Rott, and H. Thomann, “Gröbli’s solution of the three-vortex problem,” *Annual Review of Fluid Mechanics* **24**, 1–21 (1992), (see also references therein).
- [22] G. Benettin, L. Galgani, A. Giorgilli, and J.-M. Strelcyn, “Lyapunov characteristic exponents for smooth dynamical systems and for Hamiltonian systems; a method for computing all of them. part 1: Theory,” *Meccanica* **15**, 9–20 (1980).
- [23] G. Benettin, L. Galgani, A. Giorgilli, and J.-M. Strelcyn, “Lyapunov characteristic exponents for smooth dynamical systems and for Hamiltonian systems; a method for computing all of them. part 2: Numerical application,” *Meccanica* **15**, 21–30 (1980).
- [24] C. Skokos, “The Lyapunov characteristic exponents and their computation,” in *Dynamics of Small Solar System Bodies and Exoplanets*, Lecture Notes in Physics No. 790, edited by J. J. Souchay and R. Dvorak (Springer Berlin Heidelberg, 2010) pp. 63–135.
- [25] C. Froeschlé, E. Lega, and R. Gonczi, “Fast Lyapunov indicators. application to asteroidal motion,” *Celestial Mechanics and Dynamical Astronomy* **67**, 41–62 (1997).
- [26] C. Froeschlé, R. Gonczi, and E. Lega, “The fast Lyapunov indicator: a simple tool to detect weak chaos. application to the structure of the main asteroidal belt,” *Planetary and Space Science Asteroids, Comets, Meteors 1996 - II*, **45**, 881–886 (1997).
- [27] R. Barrio, “Sensitivity tools vs. poincaré sections,” *Chaos, Solitons & Fractals* **25**, 711–726 (2005).
- [28] R. Barrio, “Painting chaos: A gallery of sensitivity plots of classical problems,” *Int. J. Bifurcation Chaos* **16**, 2777–2798 (2006).
- [29] C. Skokos, “Alignment indices: a new, simple method for determining the ordered or chaotic nature of orbits,” *Journal of Physics A: Mathematical and General* **34**, 10029 (2001).
- [30] C. Skokos, T. C. Bountis, and C. Antonopoulos, “Geometrical properties of local dynamics in Hamiltonian systems: The generalized alignment index (GALI) method,” *Physica D: Nonlinear Phenomena* **231**, 30–54 (2007).
- [31] P. M. Cincotta and C. Simó, “Simple tools to study global dynamics in non-axisymmetric galactic potentials - I,” *Astronomy and Astrophysics Supplement Series* **147**, 205–228 (2000).
- [32] P. M. Cincotta, C. M. Giordano, and C. Simó, “Phase space structure of multi-dimensional systems by means of the mean exponential growth factor of nearby orbits,” *Physica D: Nonlinear Phenomena* **182**, 151–178 (2003).
- [33] Z. Sándor, B. Érdi, and C. Efthymiopoulos, “The phase space structure around l4 in the restricted three-body problem,” *Celestial Mechanics and Dynamical Astronomy* **78**, 113–123 (2000).
- [34] Z. Sándor, B. Érdi, A. Széll, and B. Funk, “The relative Lyapunov indicator: An efficient method of chaos detection,” *Celestial Mechanics and Dynamical Astronomy* **90**, 127–138 (2004).
- [35] J. Laskar, “The chaotic motion of the solar system: A numerical estimate of the size of the chaotic zones,” *Icarus* **88**, 266–291 (1990).
- [36] J. Laskar, “Frequency analysis for multi-dimensional systems. global dynamics and diffusion,” *Physica D: Nonlinear Phenomena* **67**, 257–281 (1993).
- [37] G. A. Gottwald and I. Melbourne, “A new test for chaos in deterministic systems,” *Proc. R. Soc. Lond. A* **460**, 603–611 (2004).
- [38] G. A. Gottwald and I. Melbourne, “Testing for chaos in deterministic systems with noise,” *Physica D: Nonlinear Phenomena* **212**, 100–110 (2005).
- [39] F. Ginelli, P. Poggi, A. Turchi, H. Chaté, R. Livi, and A. Politi, “Characterizing dynamics with covariant Lyapunov vectors,” *Phys. Rev. Lett.* **99**, 130601 (2007).
- [40] C. L. Wolfe and R. M. Samelson, “An efficient method for recovering Lyapunov vectors from singular vectors,” *Tellus A* **59**, 355–366 (2007).
- [41] N. P. Maffione, L. A. Darriba, P. M. Cincotta, and C. M. Giordano, “A comparison of different indicators of chaos based on the deviation vectors: application to symplectic mappings,” *Celest Mech Dyn Astr* **111**, 285–307 (2011).
- [42] L. A. Darriba, N. P. Maffione, P. M. Cincotta, and C. M. Giordano, “Comparative study of variational chaos indicators and ODEs’ numerical integrators,” *International Journal of Bifurcation and Chaos* **22**, 1230033 (2012).
- [43] C. Skokos, C. Antonopoulos, T. C. Bountis, and M. N. Vrahatis, “How does the smaller alignment index (SALI) distinguish order from chaos?” *Progress of Theoretical Physics Supplement* **150**, 439–443 (2003).
- [44] C. Skokos, C. Antonopoulos, T. C. Bountis, and M. N. Vrahatis, “Detecting order and chaos in Hamiltonian systems by the SALI method,” *Journal of Physics A: Mathematical and General* **37**, 6269 (2004).
- [45] A. Széll, B. Érdi, Z. Sándor, and B. Steves, “Chaotic and stable behaviour in the caledonian symmetric four-body problem,” *Monthly Notices of the Royal Astronomical Society* **347**, 380–388 (2004).
- [46] T. Bountis and C. Skokos, “Application of the SALI chaos detection method to accelerator mappings,” *Nuclear Instruments and Methods in Physics Research Section A: Accelerators, Spectrometers, Detectors and Associated Equipment Proceedings of the Workshop on High Intensity Beam Dynamics COULOMB 2005 Workshop on High Intensity Beam Dynamics*, **561**, 173–179 (2006).
- [47] C. Antonopoulos, T. Bountis, and C. Skokos, “Chaotic dynamics of n-degree of freedom Hamiltonian systems,” *International Journal of Bifurcation and Chaos* **16**, 1777–1793 (2006).
- [48] R. Capuzzo-Dolcetta, L. Leccese, D. Merritt, and A. Vicari, “Self-consistent models of cuspy triaxial galaxies with dark matter halos,” *The Astrophysical Journal* **666**, 165 (2007).
- [49] M. Macek, P. Stránský, P. Cejnar, S. Heinze, J. Jolie, and J. Dobeš, “Classical and quantum properties of the semiregular

- arc inside the casten triangle,” *Physical Review C* **75**, 064318 (2007).
- [50] P. Stránský, P. Hruška, and P. Cejnar, “Quantum chaos in the nuclear collective model: Classical-quantum correspondence,” *Physical Review E* **79**, 046202 (2009).
 - [51] C. Antonopoulos, V. Basios, and T. Bountis, “Weak chaos and the “melting transition” in a confined microplasma system,” *Physical Review E* **81**, 016211 (2010).
 - [52] T. Manos and E. Athanassoula, “Regular and chaotic orbits in barred galaxies – i. applying the SALI/GALI method to explore their distribution in several models,” *Monthly Notices of the Royal Astronomical Society* **415**, 629–642 (2011).
 - [53] J. Boreux, T. Carletti, C. Skokos, and M. Vittot, “Hamiltonian control used to improve the beam stability in particle accelerator models,” *Communications in Nonlinear Science and Numerical Simulation* **17**, 1725–1738 (2012).
 - [54] J. Boreux, T. Carletti, C. Skokos, Y. Papaphilippou, and M. Vittot, “Efficient control of accelerator maps,” *International Journal of Bifurcation and Chaos* **22**, 1250219 (2012).
 - [55] P. Benítez, J. C. Losada, R. M. Benito, and F. Borondo, “Analysis of the full vibrational dynamics of the LiNC/LiCN molecular system,” in *Progress and Challenges in Dynamical Systems*, Springer Proceedings in Mathematics & Statistics No. 54, edited by S. Ibáñez, J. S. P. d. Río, A. Pumariño, and J. Á. Rodríguez (Springer Berlin Heidelberg, 2013) pp. 77–88.
 - [56] C. Antonopoulos, V. Basios, J. Demongeot, P. Nardone, and R. Thomas, “Linear and nonlinear arabesques: A study of closed chains of negative 2-element circuits,” *International Journal of Bifurcation and Chaos* **23**, 1330033 (2013).
 - [57] A. J. Lichtenberg and M. A. Lieberman, *Regular and chaotic dynamics* (Springer-Verlag, New York, 1992).
 - [58] We note that the integration of the orbit and of the two deviation vectors needed for the computation of the SALI is done by using the DOPRI853 integrator[62].
 - [59] S. Middelkamp, P. G. Kevrekidis, D. J. Frantzeskakis, R. Carretero-González, and P. Schmelcher, “Bifurcations, stability, and dynamics of multiple matter-wave vortex states,” *Physical Review A* **82**, 013646 (2010).
 - [60] D. J. Frantzeskakis, “Dark solitons in atomic Bose–Einstein condensates: from theory to experiments,” *Journal of Physics A: Mathematical and Theoretical* **43**, 213001 (2010).
 - [61] S. Komineas, “Vortex rings and solitary waves in trapped Bose-Einstein condensates,” *The European Physical Journal Special Topics* **147**, 133–152 (2007).
 - [62] E. Hairer, S. P. Nørsett, and G. Wanner, *Solving Ordinary Differential Equations I - Nonstiff Problems*, 2nd ed. (Springer, 1993).